

# Combining Multi-material Rapid Prototyping and Pseudo-Rigid Body Modeling for a New Compliant Mechanism

Arnaud Bruyas, François Geiskopf, Laurence Meylheuc and Pierre Renaud

a.bruyas@unistra.fr

AVR Team, ICube

CNRS, University of Strasbourg, INSA Strasbourg

**Abstract**—Multi-Material Rapid Prototyping (MM-RP) is a promising fabrication process for compliant mechanisms, for instance when compactness is a concern. The Pseudo-Rigid Body Model (PRBM) approach is well-known for the synthesis of compliant mechanisms. It is usually based on the use of compliant joints to provide the mechanism mobilities. In this paper, we propose the HSC joint as a new type of revolute compliant joint that is well adapted to MM-RP, and that offers interesting properties in terms of stiffness and range of motion. Based on the HSC joint, a new compliant mechanism, suitable for interventional MRI, is introduced with assessment of a first prototype that is entirely made out of a single polymer part. The interest is twofold. First, the device constitutes a promising solution in this medical context. Second, the impact of the use of MM-RP in combination with PRBM can be evaluated, and their use is discussed as a conclusion.

## I. INTRODUCTION

### A. Multi-material rapid prototyping for new robotic architectures

In several contexts, the design of robotic systems still represents a challenge in terms of compactness, accuracy, or specific requirements such as compatibility with imaging devices in a medical environment. MRI scanners are for instance very interesting devices for performing image-guided procedures because of the absence of ionizing radiation and the high level of contrast of soft tissues. So-called interventional MRI (iMRI) is however a challenging technique because of the lack of space and the complexity of the medical task. It can therefore benefit from the introduction of robotics. Several robotic devices have been proposed for these kinds of procedures [1]–[4]. These devices have several degrees of freedom in order to control and insert a needle. Because of the strong magnetic field and the sensitivity of the scanner to any active element, the design of a robotic system is difficult, and the proposed solutions sometimes lack compactness.

One way to improve this situation is to consider remote actuation, as considered in [5]–[7]. The structure of the robotic devices has also to be preferably made out of polymer materials, so that MRI compatibility is ensured [8]. In the iMRI context, the system accuracy is also required. Compliant systems are therefore well-adapted to eliminate backlash, end-effector displacements being obtained thanks to the elasticity of the part materials. Conventional manufacturing of polymer materials with machining or injection molding may however not be usable for the complex geometries required

by a compliant mechanism. We therefore consider Rapid Prototyping (RP) techniques as of particular interest. In order to obtain mobilities of large amplitudes, Multi Material Rapid Prototyping (MM-RP) can be employed, especially as it is now commercially available in the case of the Polyjet 3D system [9], [10]. An interesting combination of accuracy, homogeneity of the part, mechanical properties and multi-material production capability is then obtained.

### B. Rapid prototyping in the design of robotic systems

RP techniques allows the designer to obtain three-dimensional parts with almost arbitrary shapes [10]. These additive manufacturing processes overcome complex manufacturing sequences on the shop floor [11]. As a consequence, the impact of such processes on the design of robotic systems has been investigated. First, non-assembled robotic joints have been designed [12]. Compliant joints have also been manufactured [13], [14], but for small displacements only.

Shape Deposition Manufacturing (SDM, [15]) has opened the way to produce multi-material parts using RP. Initially considered for metals, SDM can be considered to produce parts made out of different polymer materials [11] that also embed active elements. Clark et al. [16] embed wires and servos inside the structure of a biomimetic robot using SDM and manufacture its legs with a multi-material compliant structure. In terms of the design process, a biomimetic approach leads to the selection of the robot architecture, as well as the definition of the leg structures.

In the synthesis of compliant mechanisms, an efficient and widely-used method is the Pseudo-Rigid-Body Model approach (PRBM [17], [18]). Its principle is to consider the mechanism synthesis with a rigid-body mechanism, and then replace conventional joints by compliant joints. The mechanism can then be analyzed with the usual tools for rigid-body models. This method has been successfully applied in the design of compliant mechanisms [17], using flexural elements as compliant joints. It seems of interest to use such a design process for mechanisms obtained with MM-RP, but compliant joints taking advantage of MM-RP have first to be built.

In this paper, a new compliant multi-material joint is therefore proposed in a first step. Large rotations for this revolute joint can be obtained thanks to MM-RP with interesting stiffness properties. The synthesis of a mechanism using a PRBM approach is conducted in a second step. The design

case comes from the iMRI context. This allows us to provide an interesting mechanism for the application, including a first prototype. At the same time, the interest of coupling MM-RP and PRBM in the design process can be discussed and opens new perspectives, as outlined in the conclusion.

## II. DESIGN OF A COMPLIANT MULTI-MATERIAL REVOLUTE JOINT

### A. Objectives of the design

We consider in a first step the design of a revolute joint, largely used in compliant mechanisms, obtained with MM-RP. Following classical notations [18], [19], the axis of the revolute joint is defined as the Z axis. The desired behavior of a compliant revolute joint can be expressed using a compliance matrix  $C$ . It relates a set of forces and moments  $F$  applied at the center of the joint  $O$ , to a the set of translational and rotational displacements  $x$ , such as:

$$x = C.F \quad (1)$$

with  $C$  a  $6 \times 6$  matrix, which first three diagonal components relate forces and translations, and the last three diagonal components relate moments and rotations.

For a perfect compliant revolute joint,  $C$  is diagonal, such that  $C = \text{diag}(c_i)$ ,  $i \in [1, 6]$  and  $c_6$  is the only non-zero value for a Z-axis joint. The value of this coefficient depends on the application. The design objectives are therefore here to obtain a revolute joint that exhibits no extra-diagonal terms, *i.e.* no cross-coupling, and low ratios between the coefficients  $c_i$ ,  $i \in [1, 5]$ , and  $c_6$ .

Usually, the design of a compliant joint is performed assuming small strains in the material. When a single material is used in a compliant joint, all the coefficients of  $C$  are linearly dependent on the Young's modulus  $E$  of the material. To create relative variations between the values of  $C$ , it is necessary to modify the shape of the joint. Using MM-RP, the shape and the distribution of the different materials in the joint can affect the values of the compliant matrix. It is therefore required to first characterize the mechanical properties of these materials.

### B. Material characterization

In order to simplify the design issue, a combination of only two materials is considered. More precisely, among the materials that are compatible with the Polyjet technology, the materials with the highest (Material A, VeroWhitePlus RGD835) and the lowest (Material B, TangoBlackPlus FLX980) Young's modulus are chosen.

Experiments show that the material A exhibits a behavior in tension close to thermoplastics, with a Young's modulus  $E = 1890$  MPa. Using norm ISO 37/7743, tension/compression tests were also performed for material B, and the results are presented in Fig. 1. In tension, the behavior is slightly non-linear due to the hyper-elasticity of the material. It presents a maximal stress of 0.72 MPa. The compression curve presents an exponential form, with a maximum stress of 7.6 MPa without any breakage. Indeed, the material has a Poisson's coefficient close to 0.5, which

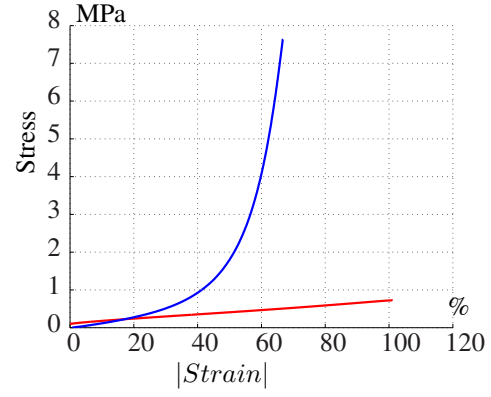


Fig. 1. Stress-strain relationships for tension (red) and compression (blue) tests on material B. Absolute value of the strain is chosen to ease the comparison of the two curves.

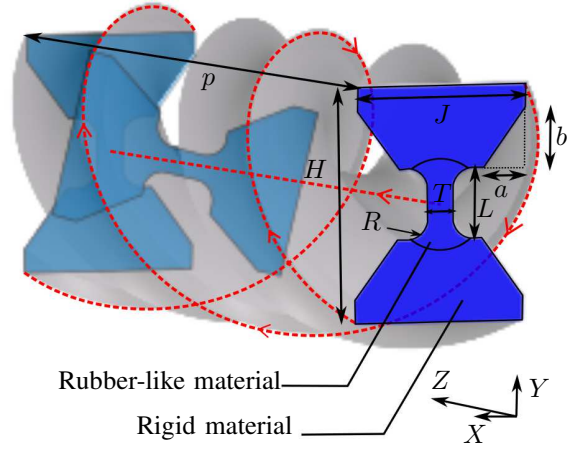


Fig. 2. Definition of the geometrical parameters of the profile of the HSC joint.

means it is incompressible. The material can be designated as a "rubber-like" material and presents a maximum strain of 70%. The compliant joint introduced in the next section is developed to take advantage of this incompressibility.

### C. The Helical Shape Compliant (HSC) joint

1) *Design principle:* Compliant joints are usually designed by extruding a flexure element. Using the rubber-like material with such joints, for instance with a circular or a corner-filletted flexural hinge, the compliance  $c_6$  would be high, as would be the compliances on the other axes. Instead of simply extruding a compliant profile in a straight way, an helical sweep around  $360^\circ$  of a flexural element is performed along a constant pitch  $p$  (see Fig. 2).

The compliant profile is normal to the Z axis, but its local orientation is spinning constantly. For any force application in the X or Y direction, there is a section along the axis that is submitted to compression. The joint stiffness is thus improved in the directions perpendicular to the joint axis. At the same time, the stiffness along the joint axis will be similar to the one obtained with an extruded profile.

With this helical sweep, the joint behavior becomes equivalent in the X and Y directions. In other words, we should

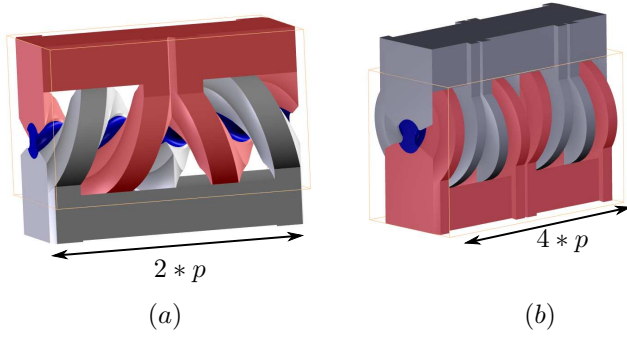


Fig. 3. Construction of the HSC Joint: (a): Two single helices with opposite pitches in parallel, (b): two patterns defined in (a) in parallel. For both of them, the blue volume is representing the rubber-like material, the grey and red ones the volumes that have a relative movement.

$H$	$J$	$R$	$T$	$L$	$a$	$b$	$p$
8	6	0.5	1.5	1.5	1.5	0.75	5

TABLE I

VALUES IN MM OF THE GEOMETRIC PARAMETERS OF THE JOINT, AS DEFINED IN FIG. 2

have  $c_2 = c_1$  and  $c_4 = c_5$ . As shown in Fig. 3(a), a joint is obtained by combining in parallel two sweeps with opposite pitches. Thus, the coupling between rotation and translation in the Z direction that is inherent to the helical shape is overcome (Fig. 3 (a)).

The geometry of the profile is adapted from a Corner-Filleted Flexure Hinge profile [19]. It is parametrized in Fig. 2. The joint geometry is also interesting because joint limits can be integrated: the maximum amplitude of the joint is defined by the values of  $a$  and  $b$ . The outside diameter of the joint is  $D = \sqrt{J^2 + H^2}$ , and the diameter of the rubber-like material is  $d = \sqrt{L^2 + (T + 2.R)^2}$ . It can be noted that several patterns can be repeated along the joint axis (Fig. 3(b)).

#### 2) Estimation of the compliance matrix by simulation:

In order to assess the behavior of the HSC joint, we have selected a specific geometry. It takes into account the minimum feasible thickness of our MM-RP technology, about 1 mm, and a large amplitude of  $\pm 45^\circ$ . The values of the set of parameters are presented in table I, and a model of the joint is presented in Fig. 3 (b). The behavior of the rubber-like material has been identified to a Yeoh model, using the results of the experiments presented in Fig. 1.

Using the CAD model of the joint, a finite element analysis (PTC Creo-Mechanica <sup>®</sup>) has been implemented. The six components of the load  $F$  have been applied separately and the displacement vector  $x$  is estimated for each load case. Small loads are applied in order to obtain small stresses. The effect of compression of the "rubber-like" material is minimized and the worst possible values of the compliances  $c_i$  are obtained.

Numerically, for a force of 2 N and a moment of 1 mm.N,

the diagonal matrix  $C_{sim}$  is obtained:

$$C_{sim} = \text{diag}(8.5e^{-5}, 9.2e^{-5}, 2.5e^{-4}, 2.8, 2.7, 256)$$

with  $c_1, c_2$  and  $c_3$  being in  $m.N^{-1}$ ; and  $c_4, c_5, c_6$  being in  $\text{rad}.N^{-1}.m^{-1}$ .

Several observations can be made from the values of  $C_{sim}$ . First,  $c_1$  and  $c_2$  are almost equal, as well as  $c_4$  and  $c_5$ , as it was expected. Moreover,  $c_6$  is almost one hundred times greater than  $c_4$  and  $c_5$ .

#### D. Experimental tests of the joint

In order to verify the previous results, joints with a geometry defined by the parameters in Table I are experimentally tested using a tension tester (Zwicker/Roell, model Z005). Three configurations are considered to sequentially apply a force in the X, Y and Z directions (directions in Fig. 2), and measure at the same time the relative displacement between the two joint ends in the same direction. Different shapes of specimens have been designed to be mountable on the tension tester. From the experimental data, values of  $c_1, c_2$  and  $c_3$  can be estimated. In each situation, tension and compression of the joints are achieved. The results are presented in Fig. 4.

The curves have similar shapes, except the two obtained in the Z direction. They are almost linear at the beginning, with a slope lower than the other graphs and a transition is happening because of the contact of the two helices. In the X and Y directions, results in tension and compression are comparable for small loads. This confirms the equivalent behavior of the joint in the X and Y directions. For large loads, discrepancies can be observed between the results of the X and Y axis. Experiments show that it is only related to the shape differences of the specimens. A comparison between simulation (black curve) and experiment (blue and cyan curve) in the Y direction shows a good correlation, with only a 10% difference on the displacement for 30 N. Moreover, these curves present an exponential shape, which confirms the influence of the "rubber-like" material incompressibility.

The HSC joint exhibits interesting properties. Large rotation is achievable, with interesting stiffnesses in the plane perpendicular to the rotational axis due to the incompressibility of the "rubber-like" material. Moreover, a symmetrical mechanical behavior is shown in this plane, because of the helical shape. Only the stiffness in the Z direction would need to be further improved. Meanwhile, the PRBM approach is applied in the following, in the sense that we will use rigid body model during the synthesis of a compliant mechanism. However, due to the non-negligible compliance in several directions, the whole matrix is used to represent the force/deflection characteristics of the joint.

### III. MECHANISM DESIGN WITH THE HSC JOINT

In the following, we consider the design of a robotic assistant for iMRI, in order to evaluate the efficiency of the new design process.

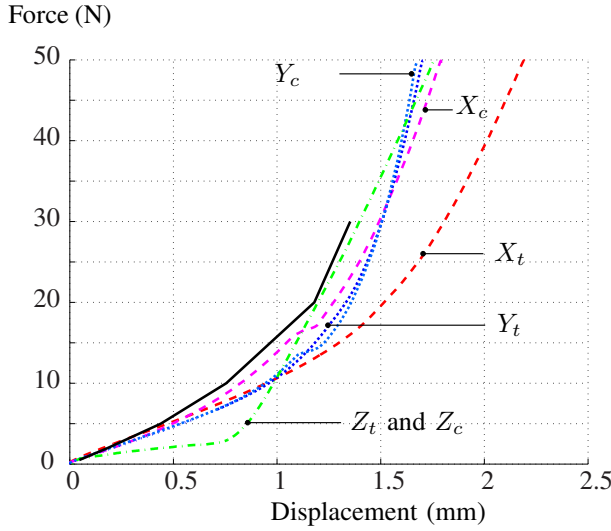


Fig. 4. Experimental test of the stiffness of the joint along the X axis (red: tension, and magenta: compression), the Y axis (blue: tension, and cyan: compression) and the Z axis (green for tension and compression), as well as the simulation results in the Y direction (black). The  $c$  and the  $t$  indices stand respectively for compression and tension

#### A. Design requirements

During percutaneous procedures in iMRI, correctly orientating the needle with respect to the patient is a difficult task. The objective is therefore to design a robotic assistant to automatically orientate a needle around its point of insertion on the skin, using MR images. As mentioned earlier, remote actuation with cables is considered. A body-mounted device is considered for the compactness it can offer, similarly to passive devices that are commercially available [20]. The device is intended to be used in two steps. First, the device positions the needle axis, in the absence of the needle. Second, the device position is maintained while the needle is manually inserted, the patient being translated to have access to the area of interest.

The device workspace can be defined as a  $90^\circ$  cone of which the apex is at the location of the incision point, and the axis is perpendicular to the skin surface (designated as the Y axis in the following). For safety reasons, it must be possible to separate the device from the needle at any time.

#### B. Mechanism selection

The mechanism synthesis with a PRBM approach is performed by first selecting the best architecture for the task. In our context, removing any physical joint from the incision location largely simplifies the cleaning of the tissues. Remote center-of-motion (RCM) architectures are therefore considered. In the same way, actuation with cables is simplified if the active joints are linked to the base of the device. As a result, we consider parallel RCM architectures.

Spherical mechanisms with RCM can be designed using revolute joints which have axes that intersect at the RCM location [21]–[23]. For large orientations, it is however difficult to avoid interferences between the legs of the mechanism. Several configurations of parallelogram-based

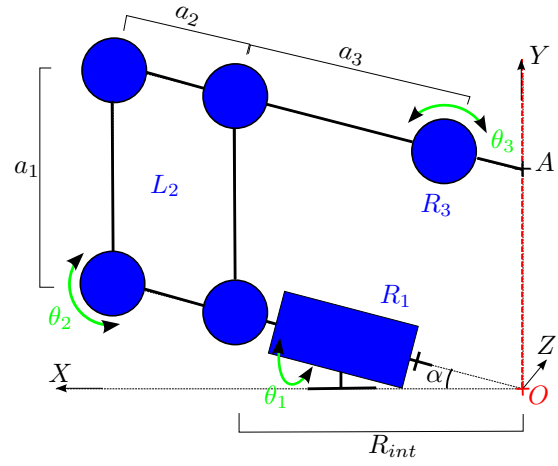


Fig. 5. A single linkage in its initial configuration, with the detail of its parameterization. Joints are represented in blue, joint variables in green and geometric parameters in black.

linkages have been presented to obtain RCM mechanisms. A list is introduced in [24], and several RCM robotic systems are based on their serial [25] or parallel [26] arrangement. A parallelogram-based architecture is chosen here, derived from the PantoScope [26]. The PantoScope is interesting because large workspaces can be obtained in the absence of singularities. The architecture we propose is based on the interconnection of two parallelogram-based linkages represented in Fig. 5 using a cylindrical joint (Fig. 6).

The needle is inserted through the cylindrical joint. This joint is necessary to obtain the two required DOF, and it is possible to design it as dismountable so that the device can be separated from the needle.

Eventually, each of the two linkages is composed of a revolute joint  $R_1$ , a parallelogram system  $L_2$  made of four revolute joints, and another revolute joint  $R_3$  in a serial arrangement (Fig. 5). The axes of the first revolute joints of the two linkages are shifted from the base plane to take into account the size of the joints and keep the RCM at the location of the incision.

#### C. The dimensional synthesis

The dimensional synthesis of the mechanism can be performed by first considering the workspace requirements. The computation of the Forward Kinematic Model (FKM) is first established for that purpose.

For a single linkage, we can define  $\theta_1$  as the angle associated to  $R_1$ ,  $\theta_2$  as the angle associated to any of the four revolute joints that compose the articulated parallelogram and  $\theta_3$  as the angle of  $R_3$ . The linkage geometry is defined by the angle  $\alpha$  between the X axis and the axis of  $R_1$  and the lengths  $a_1$ ,  $a_2$ ,  $a_3$ ,  $R_{int}$  of the different links (Fig. 5). Relationship between the joint values and the position of the point A on the needle axis can be expressed as:



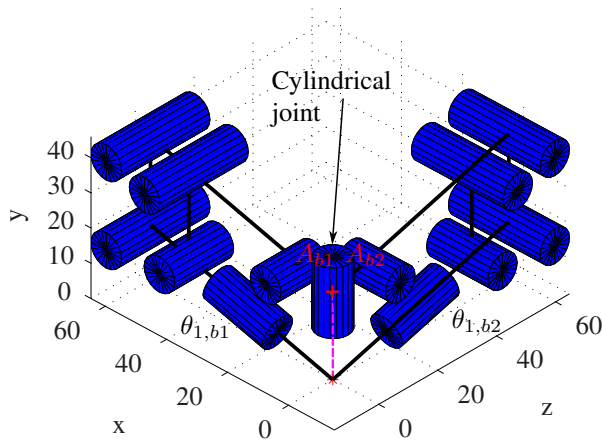


Fig. 6. Kinematic scheme of the mechanism, with  $\theta_{1,b1} = 0^\circ$  and  $\theta_{1,b2} = 0^\circ$ . In that position,  $A_{b1}$  and  $A_{b2}$  are superimposed. The magenta line is representing the needle orientation for this configuration.

$$A = R_{01} \cdot \begin{bmatrix} \left( \frac{R_{int}}{\cos(\alpha)} \right) + a_1 \cdot \sin(\alpha + \theta_2) - a_3 - d \cdot \cos(\theta_3) \\ a_1 \cdot \cos(\alpha + \theta_2) - d \cdot \sin(\theta_3) \\ 0 \end{bmatrix} \quad (2)$$

with

$$R_{01} = \begin{bmatrix} \cos(\alpha) & -\sin(\alpha) \cdot \cos(\theta_1) & -\sin(\alpha) \cdot \sin(\theta_1) \\ \sin(\alpha) & \cos(\alpha) \cdot \cos(\theta_1) & \cos(\alpha) \cdot \sin(\theta_1) \\ 0 & -\sin(\theta_1) & \cos(\theta_1) \end{bmatrix} \quad (3)$$

and

$$d = \frac{R_{int}}{\cos(\alpha)} - a_3 \quad (4)$$

Let  $(\theta_{1,b1}, \theta_{1,b2})$  be the angle of the active joints, each one being on the base of the mechanism, and  $(A_{b1}, A_{b2})$  the points that respectively belong to the first and second linkages, and to the needle axis. The FKM of the mechanism can be numerically determined by expressing that  $A_{b1}$ ,  $A_{b2}$  are aligned with the RCM  $O$  and that the coordinates of  $A_{b1}$  and  $A_{b2}$  along the Y axis are positive:

$$\overrightarrow{A_{b1}O} \cdot \overrightarrow{A_{b2}O} = 0 \quad (5)$$

According to Eq. (2), the needle angle around the X axis, linked to the Z coordinate of  $A$ , is affected by  $\theta_1$ . This is logical since the angle  $\theta_1$  defines the orientation of the plane containing  $L_2$  and  $R_3$  and therefore the needle axis. Since the workspace is defined as a  $90^\circ$  cone around the Y axis, the workspace requirements can be easily fulfilled by choosing for the two active joints a joint range equal to  $\pm 45^\circ$ .

Since compactness is a strong requirement, the geometric parameters are chosen by further considering the influence of the size of the HSC joints in the design. The design of the HSC joints has been defined in the previous section. The geometrical parameters  $(a_1, a_2, a_3, R_{int}, \alpha)$  are determined to minimize the size of the device, while avoiding any interferences for the prescribed workspace. For this purpose, a parametric CAD model is used to check for interferences.

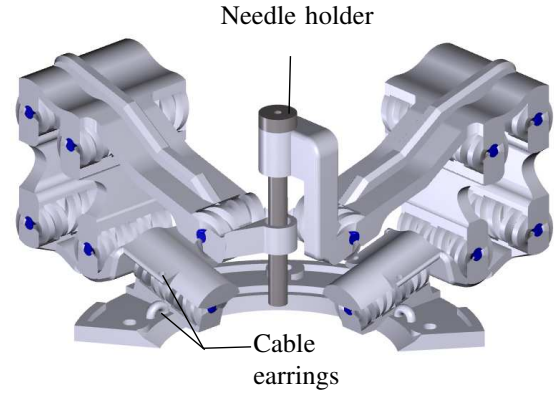


Fig. 7. CAD model of the final system (Blue color is for the rubber-like material).

Finally,  $a_1=25$  mm,  $a_2=13$  mm,  $a_3=38$  mm,  $R_{int}=47.2$  mm and  $\alpha=15^\circ$ . With such parameters, the maximal achievable angle between the needle and the Y axis, *i.e.* the needle angulation, has been estimated. Along the boundary of the workspace, this value is in average equal to  $47.4^\circ$ , which is satisfactory.

#### D. Stiffness evaluation

A compliance matrix describing the HSC joint has been numerically assessed. The stiffness of the mechanism can therefore be evaluated during the design. The method detailed in [27] is adopted, assuming that the material used for the structure is rigid. A first estimation can be performed by considering the joints on the base as non-actuated. Let  $Cf$  be the corresponding compliance matrix expressed at the point  $O$ . If we focus on the diagonal elements  $cf_i$ ,  $i \in [1, 6]$  as we did for the compliant joint:

$$cf_{1...6} = (5.5e^{-3}, 3.5e^{-3}, 5.5e^{-3}, 19.9, 2.4, 19.9)$$

The values of  $cf_4$  and  $cf_6$  are high compared to  $cf_5$ , which confirms that the device exhibits 2 DOF in rotation, with the absence of rotation along Y, the needle axis. When axial forces are applied at the incision point, the stiffnesses in the three directions are quite equivalent.

If the active joints are maintained in a static position  $(\theta_{1,b1}, \theta_{1,b2}) = (0, 0)$ , the diagonal elements of the compliance matrix  $Cb$  are equal to

$$cb_{1...6} = (4.8e^{-3}, 1.8e^{-3}, 4.8e^{-3}, 2.9, 2.3, 2.9)$$

Stiffness in rotation becomes equivalent in the three directions.

#### E. Final design

The final design is represented in Fig. 7. Revolute joints are based on the HSC joint design. The cylindrical joint uses a plain bearing described as follows: the outer cylinder is made out of PTFE and the inner tube obtained from RP. With this design, the device can be produced in a single step, directly from CAD.

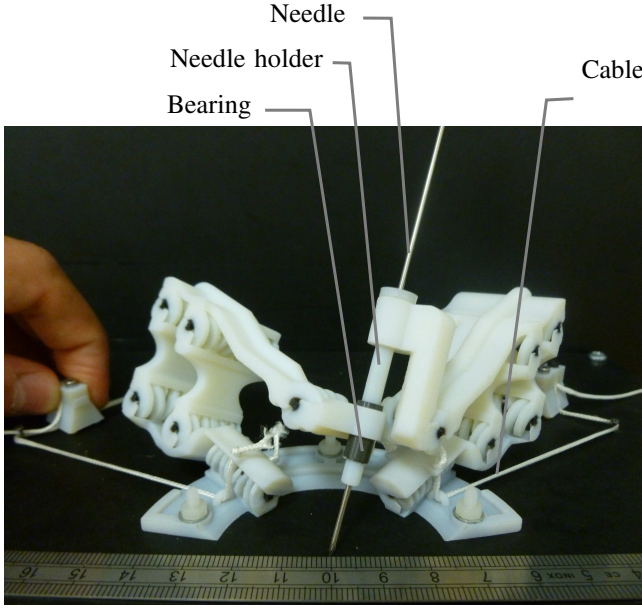


Fig. 8. Prototype of the compliant mechanism during actuation using wires. Ruler in cm.

#### IV. EXPERIMENTAL EVALUATION

##### A. Prototype manufacturing

As mentioned earlier, the whole device is produced in a single step. After cleaning, only the bearing and the wires for control need to be added. A prototype is presented in Fig. 8, shown in an actuated position.

##### B. Evaluation

The main requirements concern the amplitude of the needle rotation, and the existence of a RCM around a point that corresponds to the incision on the skin of a patient. A vision-based evaluation of the end-effector displacements is therefore performed. The principle of the evaluation is outlined in Fig. 9. The camera is positioned in two successive positions ( $O_1, B_1$ ) and ( $O_2, B_2$ ) that are chosen to put the image plane parallel to each of the two planar linkage, respectively denoted  $P_1$  and  $P_2$  in Fig. 9. Then the position of the needle axis in the image plane is recorded for several positions of the actuated joints. Two identical tests are performed. For both tests, only one active joint is activated while the other is blocked in its initial position, resulting in two series of positions (in blue and in green in fig. 9). After image processing, the position and orientation of the needle axis in the image plane ( $P'_1$  or  $P'_2$ ) is determined. The location of the center of motion  $R$  is estimated by minimizing the distance defined in Eq. (6).

$$d = \sum_{i=0}^n \text{dist}(d_i, R)^2 \quad (6)$$

Fig. 10 shows the obtained positions of the needle in the image plan  $P'_2$ , as well as the estimated center of motion  $R$ . The accuracy of the mechanism is evaluated by computing the average distance between the estimated center of motion

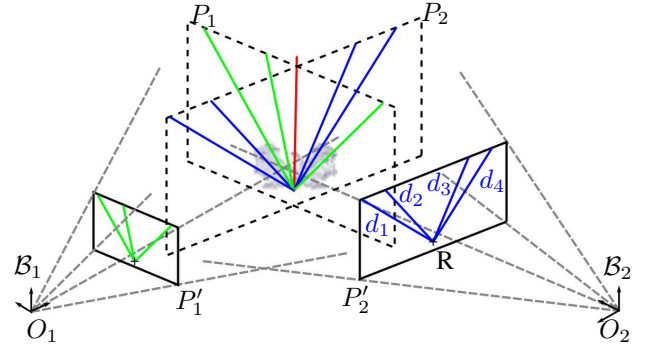


Fig. 9. Scheme of the vision based test performed to quantify the location of the center of motion of the mechanism

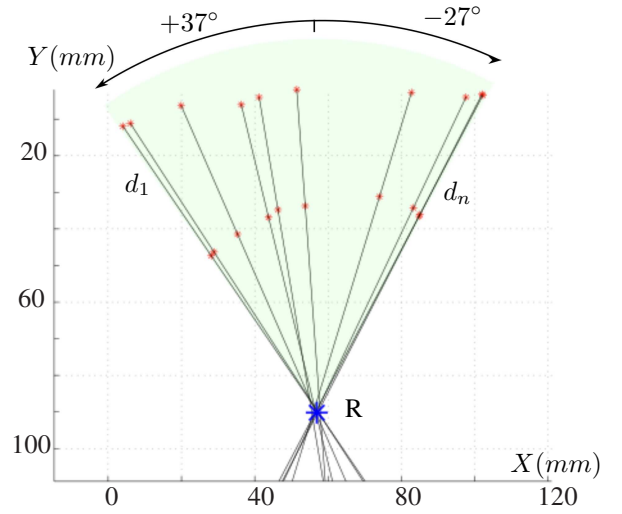


Fig. 10. Different positions of the axis of the needle, estimated center of motion  $R$  (in blue) and the angular range

$R$  and the axes  $d_i$ . This distance is equal to 0.58 mm for  $P_1$  and 0.46 mm for  $P_2$ . It seems acceptable for the application knowing that the error on the estimation of the positions of the needle is 1 pixel, which corresponds to 0.25 mm in reality.

The needle orientation can be experimentally modified in a  $(+37^\circ, -27^\circ)$  range (Fig. 10). It is lower than the value estimated during the design. One cause that has been identified is the effect of layered manufacturing: even though the layer thickness is only  $32 \mu\text{m}$  with the RP machine, the stair-step effect seems to affect the performance of the device. For a single joint, a decrease of one or two degrees on the range of motion has been observed, which is consistent with the value of the layer thickness. For the entire mechanism, several joint are combined, each one with a different orientation. This can partly explain the discrepancies. In addition, the physical stop for the range of motion is achieved with a surface/surface contact. Even the smallest imperfection on these surfaces can result in a reduction of the range of motion. In future works, the correlation between the CAD model and the prototype will be further analyzed.

## V. CONCLUSION AND FUTURE WORK

In this paper, the interest of combining MM-RP and PRBM for the design of compliant mechanisms has been investigated.

The design of the proposed HSC joint takes advantage of MM-RP, in terms of freedom of shape and material behavior. A large range of motion is obtained with interesting stiffness properties. The synthesis of a new device for iMRI is then performed following the PRBM approach. First results with the prototype make the solution of interest in the medical context, with a compact device that can be manufactured in a single step. From this example, the combination of MM-RP and PRBM in consequence appears as a promising solution to design new compliant mechanisms.

Future work will now focus first on the HSC joint properties, that need further optimization. This should indeed be performed in a global optimization to refine the joint geometry and the mechanism geometry at the same time. Such an optimization will need to take into account the existing limits of the fabrication process, such as stair-steps effects, that today affect the performances of the prototype. Further work will also be accomplished in the integration of functions around the joints in order to improve the device performances. In particular, adding braking function at the joint level would be of interest, in the medical context for example. Compliant mechanisms could then be maintained in a static position in the absence of power, which is desirable for safety reasons.

## ACKNOWLEDGMENTS

This work was supported by the Investissements d'Avenir program (Labex CAMI & Equipex ROBOTEX) under references ANR-11-LABX-0004 and ANR-10-EQPX-44.

## REFERENCES

- [1] D. Stoianovici, D. Song, D. Petrisor, D. Ursu, D. Mazilu, M. Mutener, M. Schar, and A. Patriciu, "Mri stealth robot for prostate interventions," *Minimally Invasive Therapy*, vol. 16, no. 4, pp. 241–248, 2007.
- [2] H. Elhawary, Z. T. H. Tse, A. Hamed, M. Rea, B. L. Davies, and M. U. Lamperth, "The case for mr-compatible robotics: a review of the state of the art," *Int J Med Rob. Comput Assist Surg*, vol. 4, pp. 105–113, 2008.
- [3] G. S. Fischer, I. Iordachita, C. Csoma, J. Tokuda, S. P. DiMaio, C. M. Tempany, N. Hata, and G. Fichtinger, "Mri-compatible pneumatic robot for transperineal prostate needle placement," *IEEE/ASME Trans. on Mechatronics*, vol. 13, no. 3, pp. 295–305, June 2008.
- [4] J.-S. Plante, L. Devita, K. Tadakuma, and S. Dubowsky, "Mri compatible device for robotic assisted interventions to prostate cancer," *Biomedical Applications of Electroactive Polymer Actuators*, pp. 411–425, 2009.
- [5] S. Abdelaziz, L. Esteveny, P. Renaud, B. Bayle, L. Barb, M. D. Mathelin, and A. Gangi, "Design considerations for a novel mri compatible manipulator for prostate cryoablation," *Int. J. CARS*, 2011.
- [6] A. Salimi, A. Ramezanifar, J. Mohammadpour, and K. Grigoriadis, "Gain-scheduling control of a cable-driven mri-compatible robotic platform for intracardiac interventions," *American Control Conf.*, pp. 746–751, 2013.
- [7] J. Chapuis, R. Gassert, G. Ganesh, E. Burdet, and H. Bleuler, "Investigation of a cable transmission for the actuation of mr compatible haptic interfaces," *International Conference on Biomedical Robotics and Biomechatronics*, pp. 426–431, 2006.
- [8] S. E. Song, N. B. Cho, G. Fischer, N. Hata, C. Tempany, G. Fichtinger, and I. Iordachita, "Development of a pneumatic robot for mri-guided transperineal prostate biopsy and brachytherapy: New approaches," *IEEE Int. Conf. on Rob. and Autom.*, pp. 2580–2585, 2010.
- [9] Stratasys, "Stratasys," accessed: 2013-08-30. [Online]. Available: <http://www.stratasys.com>
- [10] C. K. Chua, K. F. Leong, and C. S. Lim, *Rapid Prototyping: Principles and Applications (3rd edition)*. World Scientific Publishing, 2010.
- [11] M. R. Cutkosky and S. Kim, "Design and fabrication of multi-material structures for bioinspired robots," *Phil. Trans. R. Soc. A*, no. 367, pp. 1799–1813, 2009.
- [12] J. Won, K. DeLaurentis, and C. Mavroidis, "Rapid prototyping of robotic systems," *Proc. of IEEE Int. Conf. on Rob. and Autom.*, pp. 3077–3082, 2000.
- [13] I. Ebert-Uphoff, C. M. Gosselin, D. W. Rosen, and T. Laliberte, *Cutting Edge Robotics*. InTech, 2005, ch. Rapid Prototyping for Robotics.
- [14] S. Zhao, Y. N. Aye, C. Y. Shee, I.-M. Chen, and W. T. Ang, "A compact 3-dof compliant serial mechanism for trajectory tracking with flexures made by rapid prototyping," *Proc. of IEEE Int. Conf. on Rob. and Autom.*, pp. 4475–4480, 2012.
- [15] M. Binnard and M. R. Cutkosky, "A design by composition approach for layered manufacturing," *ASME Tran., J. Mech. Design*, vol. 122, no. 1, pp. 91–101, March 2000.
- [16] J. E. Clark, J. G. Cham, S. A. Bailey, E. M. Froehlich, P. K. Nahata, R. J. Full, and M. R. Cutkosky, "Biomimetic design and fabrication of a hexapedal running robot," *Proc. of IEEE Int. Conf. on Rob. and Autom.*, pp. 3077–3082, 2001.
- [17] L. L. Howell and A. Midha, "A method for the design of compliant mechanisms with small-length flexural pivots," *J. of Mech. Design*, vol. 116, no. 1, pp. 280–290, 1994.
- [18] L. L. Howell, *Compliant Mechanisms*. Wiley-IEEE, 2001.
- [19] N. Lobontiu, J. S. N. Paine, E. Garcia, and M. Goldfarb, "Corner-filled flexure hinges," *Trans. of the ASME*, vol. 123, pp. 346–352, Sept 2001.
- [20] NeoRad, "Simplify," accessed: 2013-08-30. [Online]. Available: [http://neorad.no/products\\_1/simplify-needle\\_holder/](http://neorad.no/products_1/simplify-needle_holder/)
- [21] M. J. H. Lum, J. Rosen, M. N. Sinanan, and B. Hannaford, "Optimization of a spherical mechanism for a minimally invasive surgical robot: Theoretical and experimental approaches," *IEEE Trans. on Biomedical Engineering*, vol. 53, no. 7, pp. 1440–1445, July 2006.
- [22] B. Hannaford, J. Rosen, D. W. Friedman, H. King, P. Roan, L. Cheng, D. Glozman, J. Ma, S. N. Kosari, and L. White, "Raven-ii: An open platform for surgical robotics research," *IEEE Trans. on Biomed. Eng.*, vol. 60, no. 4, pp. 954–959, april 2013.
- [23] F. Caron and C. Gosselin, "Two degree-of-freedom spherical orienting device," Oct. 19 1999, uS Patent 5,966,991. [Online]. Available: <https://www.google.com/patents/US5966991>
- [24] G. Zong, J. Y. X. Pei, and S. Bi, "Classification and type synthesis of 1-dof remote center of motion mechanisms," *Mechanism and Machine Theory*, vol. 43, pp. 1585–1595, 2008.
- [25] K. Y. Kim, H. S. Song, J. W. Suh, and J. J. Lee, "A novel surgical manipulator with workspace-conversion ability for telesurgery," *IEEE/ASME Trans. on Mechatronics*, vol. 18, no. 1, pp. 200–211, Feb 2013.
- [26] R. Baumann, W. Maeder, D. Glauser, and R. Clavel, "The pantoscope: A spherical remote-center-of-motion parallel manipulator for force reflection," *Proc. of Int. Conf. on Rob. and Autom.*, pp. 718–723, 1997.
- [27] Qingsong and Y. Li, "Stiffness modeling for an orthogonal 3-pu compliant parallel micromanipulator," *IEEE Proc. of Int. Conf. on Mechatronics and Autom.*, pp. 124–129, 2006.